Supplementary Information

Niobium disulphide (NbS_2)-based (heterogeneous) electrocatalysts for efficient hydrogen evolution reaction

Leyla Najafi,[a†] Sebastiano Bellani,[a†] Reinier Oropesa-Nuñez,[b] Beatriz Martín-García,[a] Mirko Prato,[c] Vlastimil Mazánek,[d] Doriana Debellis,[e] Simone Lauciello,[e] Rosaria Brescia,[e] Zdeněk Sofer,[d] and Francesco Bonaccorso*[a,b]

a *Graphene Labs, Istituto Italiano di Tecnologia, via Morego 30, 16163, Genova, Italy.*

b *BeDimensional Spa., Via Albisola 121, 16163 Genova, Italy.*

c *Materials Characterization Facility, Istituto Italiano di Tecnologia, via Morego 30, 16163 Genova, Italy.*

d *Department of Inorganic Chemistry, University of Chemistry and Technology Prague, Technická 5, 166 28 Prague 6, Czech Republic.*

e *Electron Microscopy Facility, Istituto Italiano di Tecnologia, via Morego 30, 16163 Genova, Italy*

† These authors contributed equally to this work

Scanning electron microscopy-coupled energy dispersive X-ray spectroscopy analysis of as-synthetized NbS_2 crystals

Table S1 reports the chemical composition of the as-synthetized NbS_2 crystals, corresponding to the area in the scanning electron microscopy-coupled energy dispersive X-ray spectroscopy (SEM-EDS) maps reported in the main text (**Fig. 1a-c**). As discussed in the main text, the SEM-EDS analysis revealed a near-ideal stoichiometric phase of the NbS_2 crystals (S:Nb atomic ratio ~1.8), in agreement with previous studies.[1]

Table S1. Elemental composition of the as-synthetized NbS_2 crystals obtained from SEM- EDS analysis.

Element	**atomic %**
Nb	35.4
S	64.6

X-ray photoelectron spectroscopy analysis of the NbS_2 crystals and the Nb_2 flakes

Fig. S1 reports the X-ray photoelectron spectroscopy (XPS) measurement for as-synthetized NbS_2 crystals and the NbS_2 flakes produced by liquid-phase exfoliation (LPE)[2,3] of the synthetized crystals in 2-propanol (IPA) followed by sedimentation-based separation (SBS).[4,5] The Nb 3d spectra (**Fig. S1a,b**) show the presence of three doublets. The first doublet (peaks at 203.4±0.2 eV and 206.1±0.2 eV) and the second doublet (peaks at 204.0±0.2 and 206.7±0.2 eV) may be both assigned to Nb(4+) state in NbS_2.[6,7,8,9] The origin of two doublets for NbS_2 could be ascribed to the presence of multiple NbS_2 phases, *i.e.*, *2H* (or *1H*) and *3R* ones. This has been previously observed in the most investigated MX_2, *i.e.*, MoS_2 and WS_2, in which the XPS is sensitive to the difference of the Fermi level between the *1T* and the *2H* (or *1H*) phases (the *1T* signal is downshifted by 0.8 eV relative to the *1H* phase).[10,11] Moreover, for the case of NbS_2, *3R*-NbS_2 exhibits a slight deviation from its ideal stoichiometry as consequence of an excess of Nb atoms,[12,13,14] which occupy octahedral sites between the van der Waals gaps of the S lattice,[15] resulting in Nb((4-δ)+) states (lowest binding energy doublet).[16,17] We cannot fully exclude the presence of oxidized surface states,[78] as Nb(2+) in NbO, usually contributing with peaks in the same energy range.[18,19,20] The peaks located at binding energies of 207.7±0.2 eV and 210.4±0.2 eV are assigned to the Nb(5+) state in Nb_2O_5.[18,21,22,23,24] It is worth to notice that the surface oxidation of metallic NbS_2 is a well-known effect in literature.[1,25,26] However, in agreement with Pourbaix diagram of Nb,[27] Nb_2O_5 easily can dissolve in both acidic and alkaline media to form $Nb(OH)_4^-$ and NbO_3^-, respectively. Consequently, the surface properties of the as-synthetized material can be affected by the electrochemical conditions (possibly restoring the NbS_2 surface). The S 2p spectra (**Fig. S1c,d**) show two doublets, one with peaks at 160.8±0.2 eV and 162.0±0.2 eV and the other with peaks at 161.7±0.2 eV and 162.9±0.2 eV that, in analogy with what discussed for Nb 3d, might correspond to the S $2p_{1/2}$ and S $2p_{3/2}$ peaks of the S(2-) in the two phases of NbS_2.[16,17] The remaining peak located at ~169.5 eV is associated to S(+6) in SO_4^{2-}.[28] Notably, this shows a negligible atomic weight percentage relative to the total S (~2.8%).

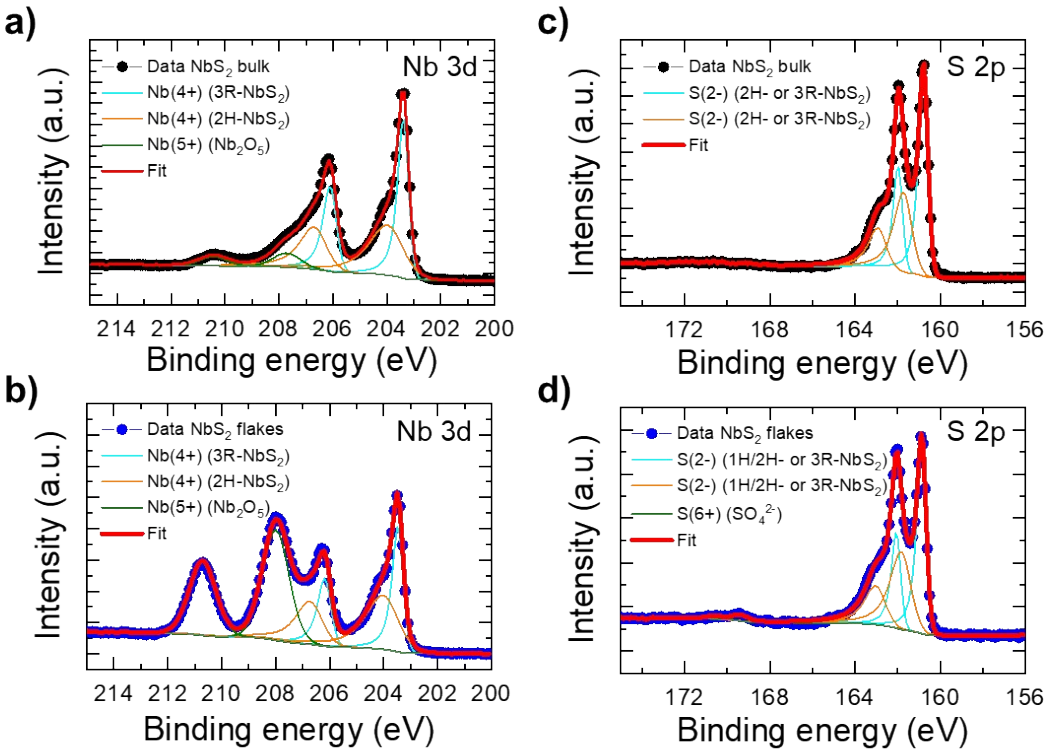

Fig. S1. a,b) Nb 3d XPS spectra of the as-synthetized NbS_2 crystal (bulk) and the LPE-produced flakes, respectively. c,d) S 2p XPS spectra of the as-synthetized NbS_2 crystal and the LPE-produced NbS_2 flakes. The deconvolutions of the spectra are also shown evidencing the bands attributed to the different oxidation states.

Scanning electron microscopy analysis of the single-walled carbon nanotubes

Fig. S2 reports the top-view scanning electron microscopy (SEM) images of the single-walled carbon nanotubes (SWCNTs) used as catalyst support. The surface of the SWCNT electrode consists of a mesoporous network forming a bundle-like morphology.

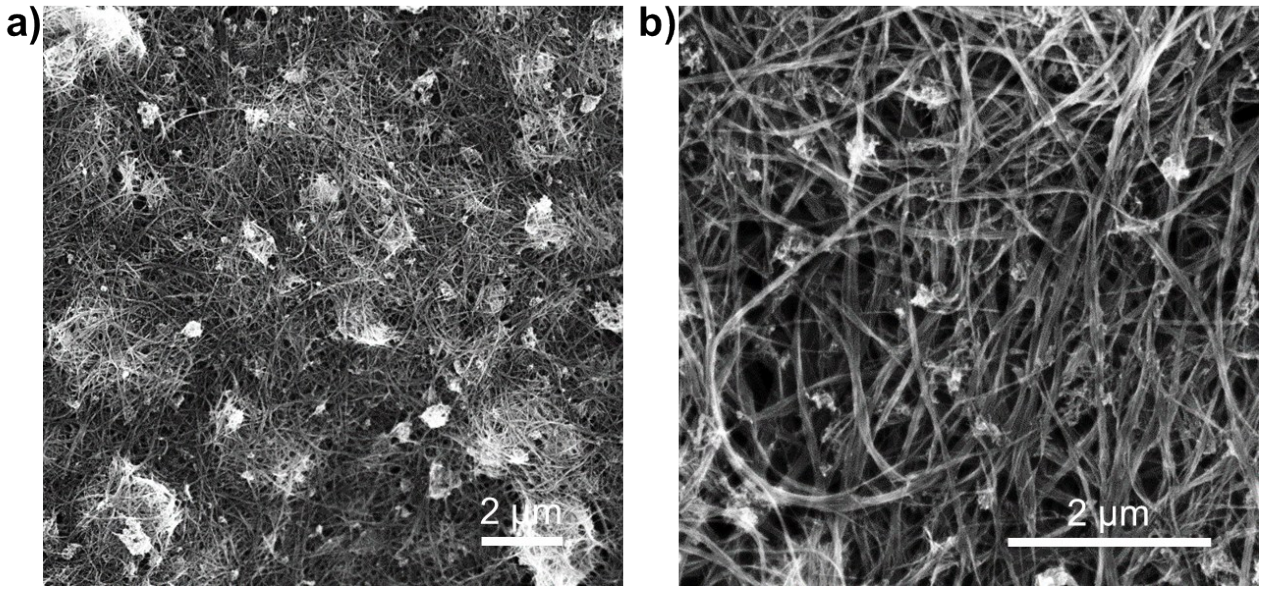

Fig. S2. a) Top-view SEM images of the SWCNTs used as catalyst support. b) Enlargement of the SEM image shown in panel a).

Scanning electron microscopy analysis of the Li–TFSI-treated NbS_2 electrode

Fig. S3 shows a top-view SEM image of the Li–TFSI-treated NbS_2 electrode, evidencing that the NbS_2 flakes are more perpendicularly oriented to the substrates relatively to the untreated NbS_2 electrodes (see **Fig. 3c** of the main text)

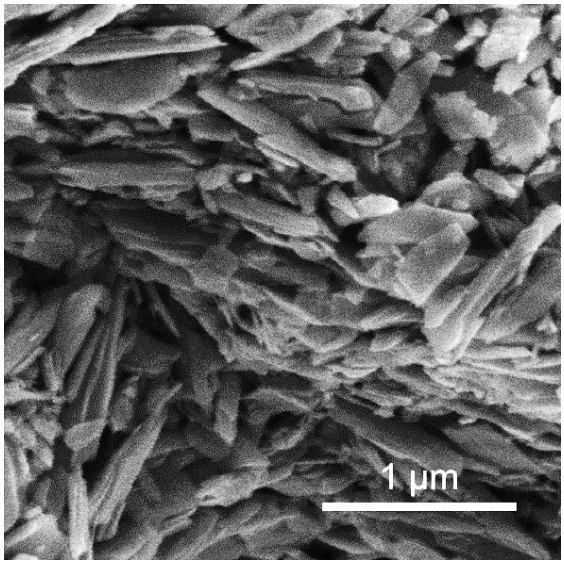

Fig. S3. Top-view SEM image of the Li–TFSI-treated NbS_2 electrode.

Double-layer capacitance measurements of the NbS_2 films

The double-layer capacitances (C_{dl}) of the untreated and treated NbS_2 films were estimated by cyclic voltammetry (CV) measurements in a non-Faradaic region of potential (between 0.2 and 0.4 V *vs.* RHE) at various potential scan rates (ranging from 20 to 600 mV s^{-1}). The NbS_2 films were deposited on glassy carbon by drop casting the as-produced NbS_2 flakes dispersion in IPA (catalyst mass loading = 0.5 mg cm^{-2}). The use of flat glassy carbon as the substrate allows the C_{dl} contribution of the substrate to be limited relatively to the case of a catalyst film deposited on SWCNTs (as for the electrodes investigated in the main text). By plotting the difference between the anodic and the cathodic current densities ($\Delta j = (j_a - j_c)$) at 0.3 V *vs.* RHE as a function of the scan rate (SR) (**Fig. S4a**), the C_{dl} was calculated by: $C_{dl} = (\Delta j)/2(SR)$. The calculated C_{dl} of the Li–TFSI –treated electrode is ~10.8 mF cm^{-2}, which is more than three orders of magnitude higher than the one of the untreated electrode. After the electrochemical treatment (1000 CV scans), the electrode (named NbS_2 – CV@1000) lost a significant amount of material, which was visible by eye (**Fig. S4b**). This effect is a consequence of the catalyst film fragmentation originated by the H_2 bubbling.[29,30,31] However, the C_{dl} of NbS_2 – CV@1000 is similar to the one of the untreated electrode, indicating that its specific electrochemically accessible surface area (defined by the ratio of the electrochemically accessible surface area and the mass loading) is significantly higher than the one of the untreated electrode.

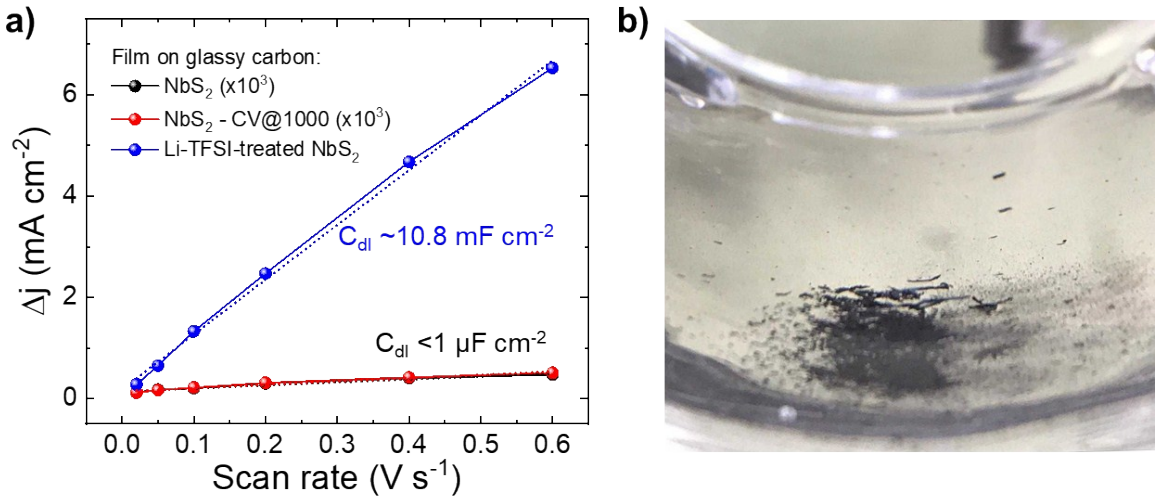

Fig. S4. a) Scan rate dependence of the Δj measured for the untreated, electrochemically treated and chemical treated NbS_2 films deposited on glassy carbon (electrode named NbS_2, NbS_2 – CV1000, Li–TFSI-treated NbS_2). The linear fits of the curves and the calculated C_{dl} values are also shown. b) Photograph showing the material losses occurred during the preparation of the NbS_2 – CV1000.

X-ray photoelectron spectroscopy analysis of the Li–TFSI-treated and electrochemically treated films of NbS_2 flakes

Fig. S5 shows the XPS spectra of the as-produced film of NbS_2 flakes and after chemical (Li-TFSI bath) and electrochemical treatments (1000 CV scans). Both the Nb 3d and the S 2p spectra (**Fig. S5a,b**, respectively) do not show significant differences attributed to a chemical composition change of the NbS_2 flakes. Compared to the as-produced film, the slight reduction of the peaks assigned to the Nb(5+) state in Nb_2O_5 (binding energies of ~207.7 and 210.4 eV)[18,21,22,23,24] after the chemical treatment could be ascribed to the stripping of the surface oxide originated by the outward diffusion of Li–TFSI when samples are exposed to air/water during their preparation. The Nb(5+) peaks also slightly reduce after the electrochemical treatments. This effect could be a consequence of the dissolution of Nb_2O_5 in acidic condition to form $Nb(OH)_4^-$, in agreement with the Pourbaix diagram of Nb.[27] The increase of the peaks associated to S(6+) in SO_4^{2-} (energy binding between~168 and 171 eV)[28] after electrochemical treatments is due to the electrolyte (H_2SO_4) residuals.

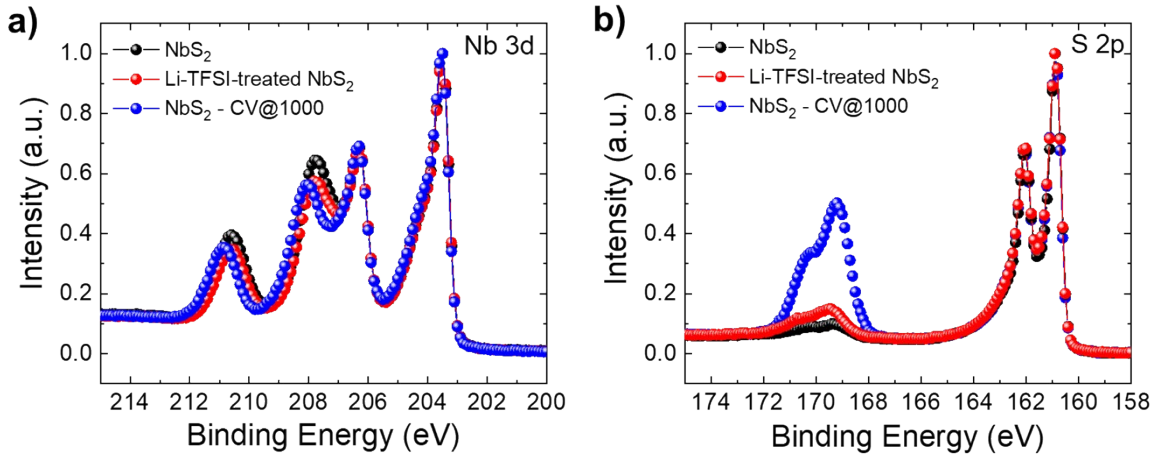

Fig. S5. a) Nb 3d and b) S 2p XPS spectra of the NbS_2 films before and after chemical and electrochemical treatment (sample named NbS_2, Li–TFSI-NbS_2 and NbS_2 – CV@1000).

Electrochemical measurements of Li–TFSI-treated NbS_2 electrodes

Fig. S6a,b show the *iR*-corrected linear sweep voltammetry (LSV) curves in 0.5 M H_2SO_4 and 1 M KOH, respectively, for a Li–TFSI-treated NbS_2 electrode before and after 1000 cyclic voltammetry cycles (electrodes named Li–TFSI-treated NbS_2 and Li–TFSI-treated NbS_2 – CV@1000 cycles, respectively). In addition, the LSV curves obtained for the as-produced NbS_2 reference and the Pt/C benchmark are also plotted. As shown for the NbS_2 reference (see **Fig. 4** of the main text), the electrochemical cycling improves the hydrogen evolution reaction (HER)-activity of the Li–TFSI treated NbS_2 electrode. In particular, their initial η_{10} (0.31 and 0.33 eV in 0.5 M H_2SO_4 and 1M KOH, respectively) increase up to 0.27 and 0.28 V in 0.5 M H_2SO_4 and 1M KOH, respectively.

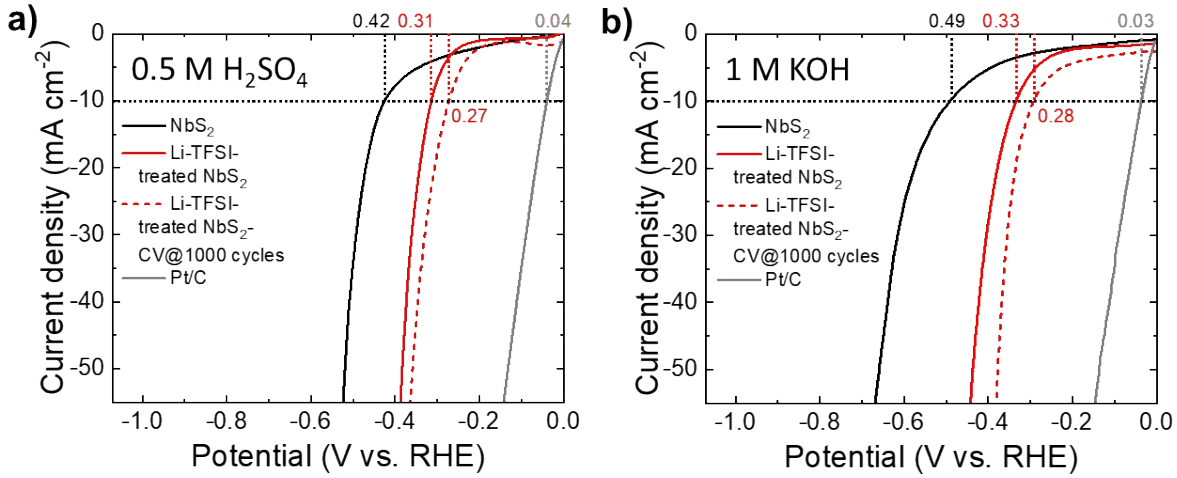

Fig. S6. a,b) *iR*-corrected LSV curves for NbS_2, Li–TFSI-treated NbS_2 and Li–TFSI-treated NbS_2 – CV@1000 cycles in acidic (0.5 M H_2SO_4) and alkaline (1 M KOH) solutions, respectively. The LSV curves of Pt/C benchmarks are also shown for comparison. The η_{10} values measured for the electrodes are also shown.

Scanning electron microscopy analysis of $MoSe_2$ and heterogeneous NbS_2:$MoSe_2$ electrodes

Fig. S7a,b show the top-view SEM images of $MoSe_2$ and heterogeneous NbS_2:$MoSe_2$ electrodes. The as-produced electrodes display a surface uniformly covered by the flakes. In particular, the heterogeneous electrode shows a morphology resembling those of $MoSe_2$ electrode, whose flakes are smaller than NbS_2 flakes, in agreement with the characterization of materials (see main text, **Fig. 1g** for NbS_2 flakes and refs. [32],[33],[34] for $MoSe_2$ flakes). This means that $MoSe_2$ flakes effectively stack up the NbS_2 flakes.

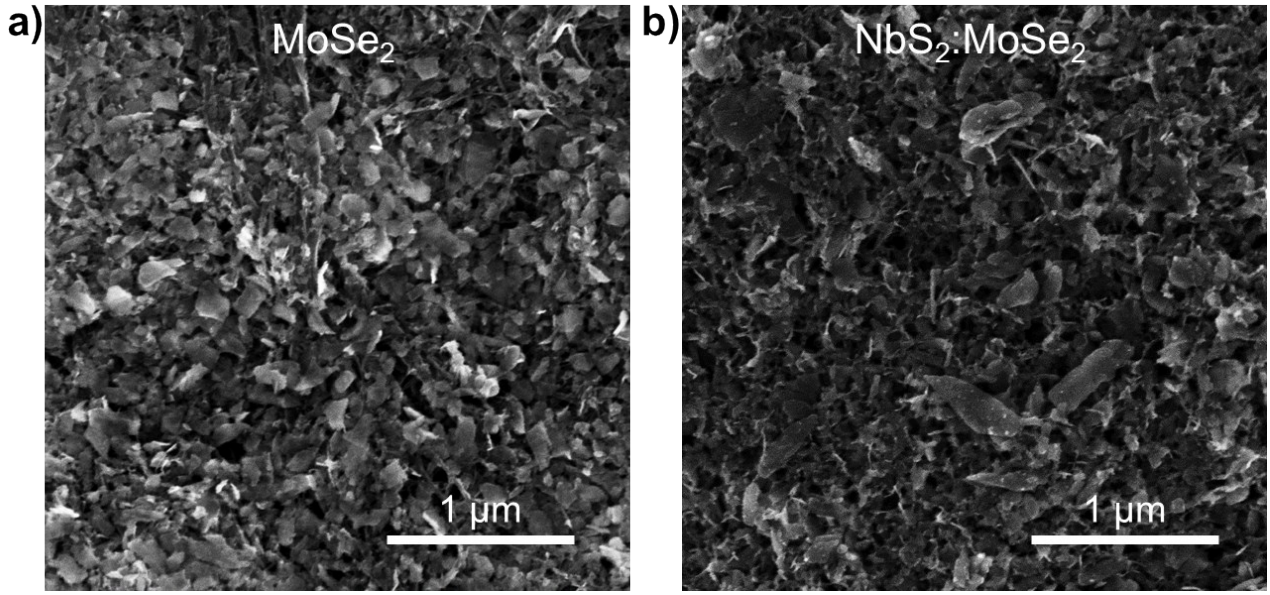

Fig. S7. a,b) Top-view SEM images of the $MoSe_2$ and NbS_2:$MoSe_2$ electrodes, respectively.

Scanning electron microscopy-coupled energy dispersive X-ray spectroscopy analysis of the NbS_2:$MoSe_2$ electrodes

Fig. S8a,b show the cross-sectional SEM-EDS analyses of the untreated NbS_2:$MoSe_2$ and the Li–TFSI-treated NbS_2:$MoSe_2$ electrodes, respectively. The data show a homogeneous distribution of both Nb and Mo elements for both the untreated NbS_2:$MoSe_2$ and the Li–TFSI-treated NbS_2:$MoSe_2$ electrodes). **Fig. S8c,d** report the top-view SEM-EDS analyses of the untreated NbS_2:$MoSe_2$ and the Li–TFSI-treated NbS_2:$MoSe_2$ electrodes, respectively. The data show homogeneous distributions of the composing elements, further suggesting the absence of single material domains.

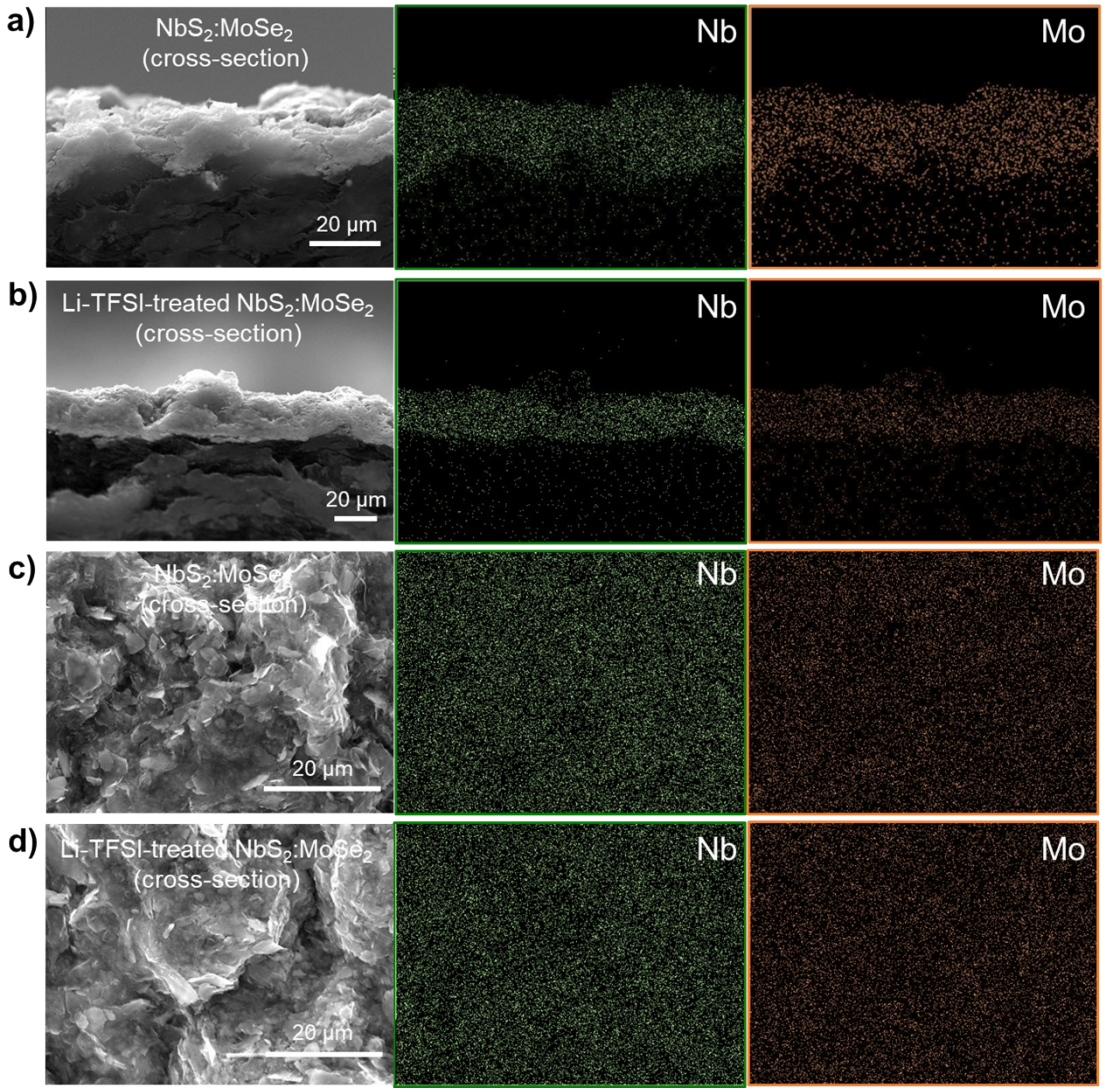

Fig. S8. a,b) Cross-section SEM images of the untreated NbS_2:$MoSe_2$ and the Li–TFSI-treated NbS_2:$MoSe_2$ electrodes, respectively, with the corresponding elemental maps for Nb (Kα peak at 16.58 keV, green) and Mo (Kα peak at 17.44 keV, orange). c,d) Top-view SEM images of the untreated NbS_2:$MoSe_2$ and the Li–TFSI-treated NbS_2:$MoSe_2$ electrodes, respectively, with the corresponding elemental maps for Nb (Kα peak, in green) and Mo (Kα peak, in orange).

Electrochemical measurements of the $MoSe_2$ electrodes

Fig. S9a,b show the *iR*-corrected LSV curves in 0.5 M H_2SO_4 and 1 M KOH, respectively, for the as-produced $MoSe_2$ electrode before and after Li–TFSI treatment (electrodes named $MoSe_2$ and Li–TFSI-treated $MoSe_2$, respectively). In addition, the LSV curves obtained for the $MoSe_2$ electrode after 1000 CV cycles (samples named $MoSe_2$ – CV@1000 cycles), the Pt/C benchmark and the SWCNTs (catalyst support) are also plotted. In 0.5 M H_2SO_4, Li–TFSI-treated $MoSe_2$ exhibits a HER-activity (η_{10} = 0.28 V) slightly higher than that of the $MoSe_2$ electrodes (η_{10} = 0.29 V). The electrochemical cycling also improves the HER-activity of the $MoSe_2$, and the $MoSe_2$ – CV@1000 cycles shows a η_{10} of 0.18 V. Similar results were also measured in 1 M KOH, in which both Li–TFSI-treated $MoSe_2$ and $MoSe_2$ – CV@1000 show a η_{10} of 0.30 V, whereas the as-produced $MoSe_2$ displays a η_{10} of 0.35 V.

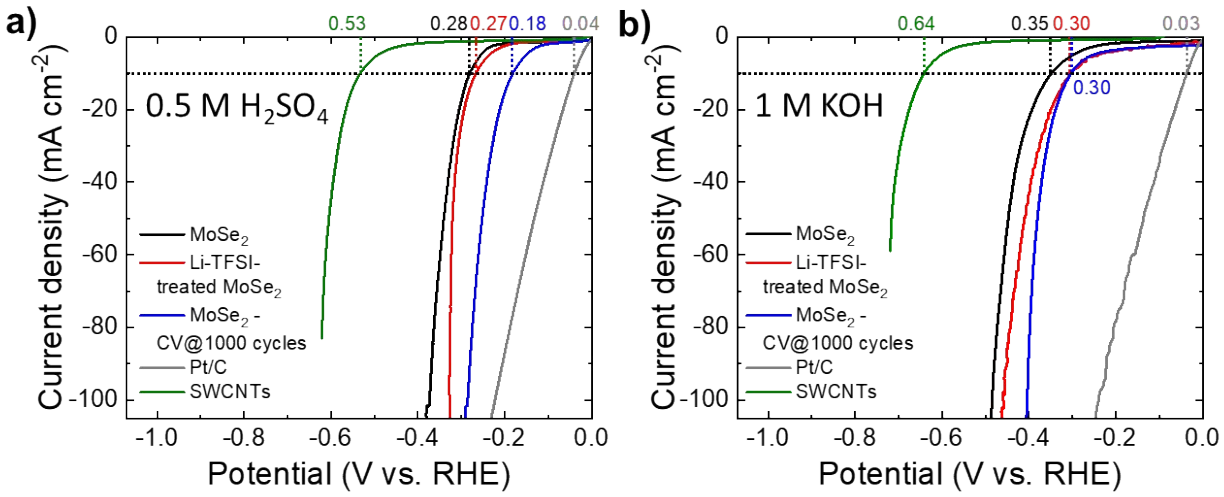

Fig. S9. a,b) *iR*-corrected LSV curves for $MoSe_2$, Li–TFSI-treated $MoSe_2$ and $MoSe_2$ – CV@1000 cycles in acidic (0.5 M H_2SO_4) and alkaline (1 M KOH) solutions, respectively. The LSV curves of Pt/C benchmark and SWCNTs (catalyst support) are also shown for comparison. The η_{10} values measured for the electrodes are also shown.

X-ray photoelectron spectroscopy measurements of the Li–TFSI-treated NbS_2:$MoSe_2$ electrodes after stability tests

Fig. S10a,b show the XPS measurements (Mo 3d/S 2s, Nb 3d and Se 3d spectral regions) of the Li–TFSI-treated NbS_2:$MoSe_2$ electrodes after stability tests (*i.e.*, chronoamperometry measurements at a fixed potential corresponding to an initial cathodic current density of 80 mA cm^{-2} for 12 h) in 0.5 M H_2SO_4 and 1 M KOH, respectively. As shown in **Fig. S10a**, the data show that both the NbS_2 and the $MoSe_2$ flakes retain their initial chemical compositions under HER-operation in acidic conditions. In fact, the Nb 3d spectrum resembles the one measured for the as-produced NbS_2 flakes (see **Fig. S1b**), while the Mo 3d spectrum instead shows the component attributed to Mo(4+) in $MoSe_2$.[32,33] The S 2s XPS spectrum shows the peak attributed to the S(2-) in NbS_2, while the peaks in the Se 3d spectrum refer to Se(2-) in the $MoSe_2$.

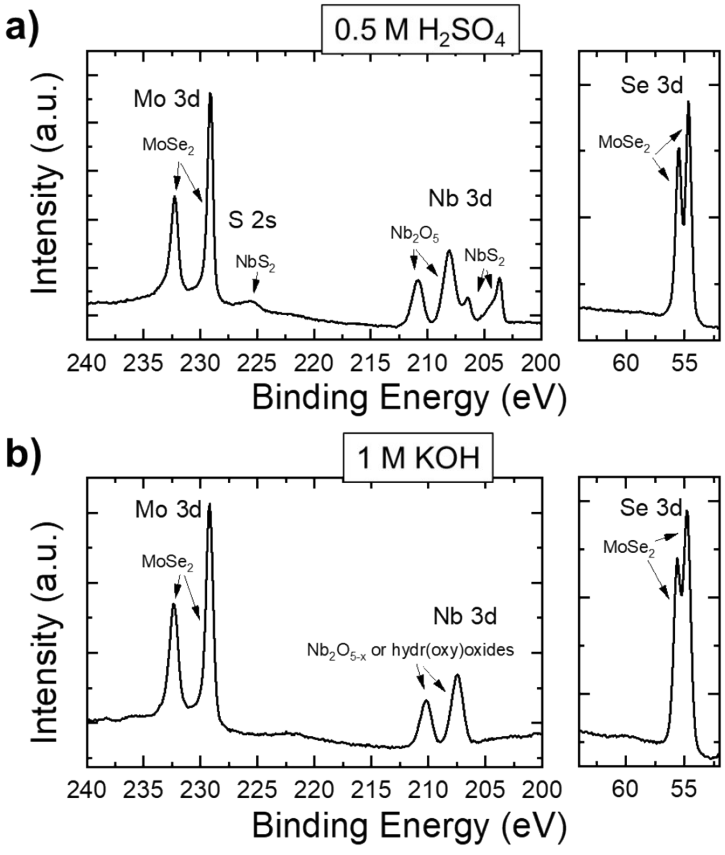

Fig. S10. a,b) Mo 3d, S 2s, Nd 3d and Se 3d XPS spectra of Li–TFSI-treated NbS_2:$MoSe_2$ electrodes after stability tests in 0.5 M H_2SO_4 and 1 M KOH, respectively.

Noteworthy, the data of the electrode tested in alkaline conditions do not show the band attributed to NbS_2 in both Nb 3d and S 2s spectra, while, on the contrary, the bands attributed to the $MoSe_2$ flakes

are displayed. Moreover, the peaks shown in the Nb 3d spectrum are located at lower energy compared to those of Nb_2O_5. Therefore, sub-stoichiometric Nb_2O_{5-x} or hydr(oxy)oxides species are suggested to be formed during the HER-operation in such condition. Contrary, the peaks in the Mo 3d spectrum are those attributed to $MoSe_2$ flakes, which are stable in alkaline condition (in agreement with previous studies).[32,33]

Scanning electron microscopy-coupled energy dispersive X-ray spectroscopy analysis of the Li–TFSI-treated NbS_2:$MoSe_2$ electrodes after stability tests in 1 M KOH

Fig. S11a,b show the cross-sectional and top-view SEM-EDS analysis of the Li–TFSI-treated NbS_2:$MoSe_2$ electrode after the stability test in 1 M KOH. Their atomic element analysis reveals a significant decrease of Nb:Mo atomic ratio, as can be seen in the evolution of their respective Kα lines in the EDS spectra, compared to the one of the as-produced electrodes (**Fig. S11c**). These results indicate a progressive loss of NbS_2 flakes. In agreement with the XPS analysis (see **Fig. S10**), NbS_2 flakes can be oxidized to form Nb_2O_5. The latter is expected to dissolve in alkaline media to form NbO_3^-,[27] as well as hydr(oxy)oxides that can then interact synergistically with $MoSe_2$ flakes to perform the HER process.[32,33,35]

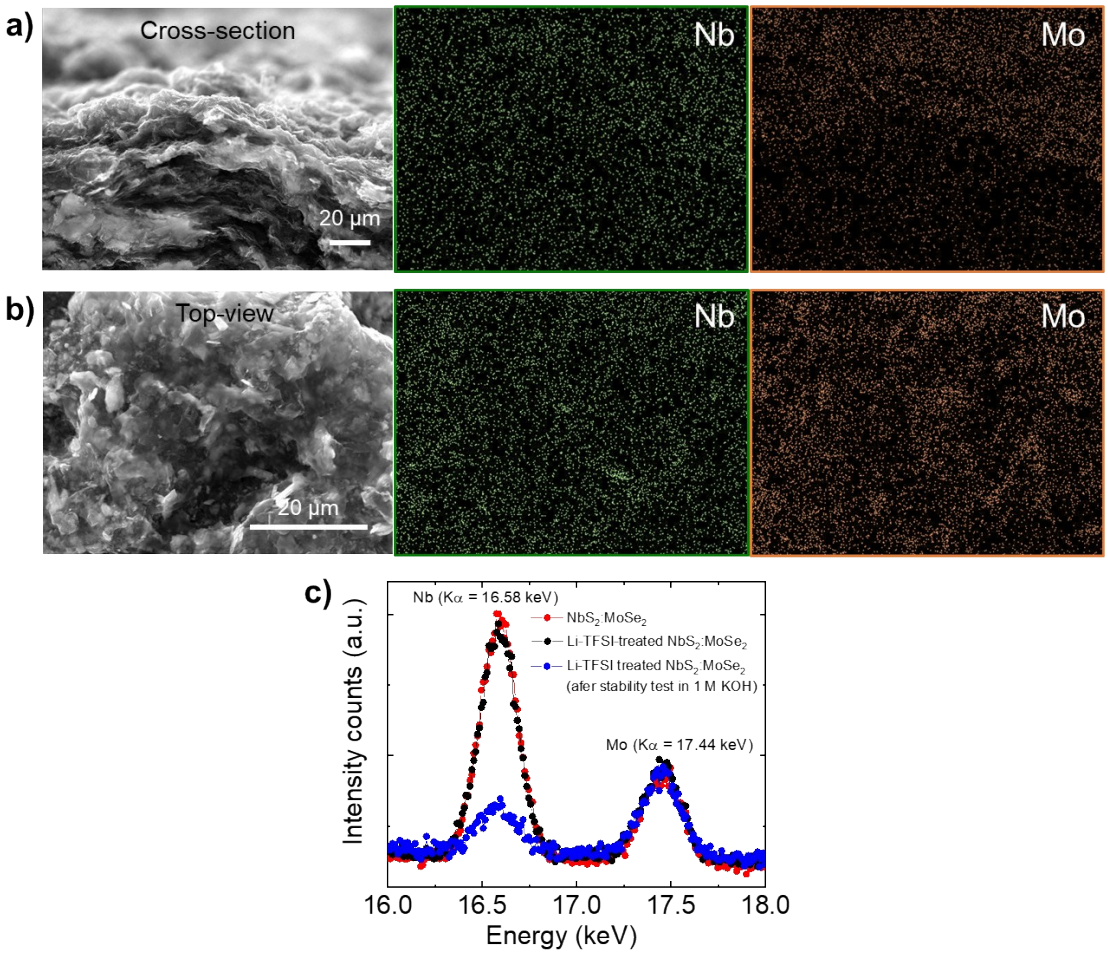

Fig. S11. a) Cross-section and b) top-view SEM images of the Li–TFSI-treated NbS_2:$MoSe_2$ electrode after stability test in 1 M KOH, with the corresponding EDS elemental map for Nb (Kα peak at 16.58 keV, in green), and Mo (Kα peak at 17.44 keV, in orange). c) Evolution of the EDS spectra for the Nb (Kα peak), and Mo (Kα peak) from the starting electrode (red), after the Li-TFSI treatment (black) and after the stability test in 1 M KOH.

Notes and references

1 X. Chia, A. Ambrosi, P. Lazar, Z. Sofer and M. Pumera, *J. Mater. Chem. A*, 2016, **4**, 4241–14253.

2 F. Bonaccorso, A. Bartolotta, J. N. Coleman and C. Backes, *Adv. Mater.*, 2016, **28**, 6136–6166.

3 V. Nicolosi, M. Chhowalla, M. G. Kanatzidis, M. S. Strano and J. N. Coleman, *Science*, 2013, **340,** 1226419.

4 A. Capasso, A. E. Del Rio Castillo, H. Sun, A. Ansaldo, V. Pellegrini and F. Bonaccorso, *Solid State Commun.*, 2015, **224**, 53–63.

5 O. M. Maragó, F. Bonaccorso, R. Saija, G. Privitera, P. G. Gucciardi, M. A. Iatì, G. Calogero, P. H. Jones, F. Borghese, P. Denti, V. Nicolosi and A. C. Ferrari, *ACS Nano*, 2010, **4**, 7515–7523.

6 J. K. Dash, L. Chen, P. H. Dinolfo, T. M. Lu and G. C. Wang, *J. Phys. Chem. C*, 2015, **119**, 19763-19771.

7 X. Zhou, S.-H. Lin, X. Yang, H. Li, M. N. Hedhili, L.-J. Li, W. Zhang and Y. Shi, *Nanoscale*, 2018, **10**, 3444–3450.

8 H. Bark, Y. Choi, J. Jung, J. H. Kim, H. Kwon, J. Lee, Z. Lee, J. H. Cho and C. Lee, *Nanoscale*, 2018, **10**, 1056-1062.

9 J. Zhang, C. Du, Z. Dai, W. Chen, Y. Zheng, B. Li, Y. Zong, X. Wang, J. Zhu and Q. Yan, *ACS Nano*, 2017, **11**, 10599–10607.

10 C. A. Papageorgopoulos and W. Jaegermann, *Surf. Sci.*, 1995, **338**, 83–93.

11 M. Saber, G. Khabiri, A. Maarouf, M. Ulbricht, A. Khalil and M. Saber R., *A comparative study on the photocatalytic degradation of organic dyes using hybridized 1T/2H, 1T/3R and 2H MoS 2 nano-sheets*, 2018, vol. 8.

12 W. G. Fisher and M. J. Sienko, *Inorg. Chem.*, 1980, **19**, 39–43.

13 F. Kadijk and F. Jellinek, *J. Less Common Met.*, 1969, **19**, 421–430.

14 F. Jellinek, G. Brauers and H. Muller, *Nature*, 1960, **185**, 376–377.

15 D. R. Powell and R. A. Jacobson, *J. Solid State Chem.*, 1981, **37**, 140–143.

16 X. Ou, X. Xiong, F. Zheng, C. Yang, Z. Lin, R. Hu, C. Jin, Y. Chen and M. Liu, *J. Power Sources*, 2016, **325**, 410–416.

17 K. Izawa, S. Ida, U. Unal, T. Yamaguchi, J.-H. Kang, J.-H. Choy and Y. Matsumoto, *J. Solid State Chem.*, 2008, **181**, 319–324.

18 M. K. Bahl, *J. Phys. Chem. Solids*, 1975, **36**, 485–491.

19 M. V. Kuznetsov, A. S. Razinkin and E. V. Shalaeva, *J. Struct. Chem.*, 2009, **50**, 514–521.

20 K. Kowalski, A. Bernasik, W. Singer, X. Singer and J. Camra, in *Proceedings of SRF2003*, 2003.

21 K. Kim, M. S. Kim, P. R. Cha, S. H. Kang and J. H. Kim, *Chem. Mater.*, 2016, **28**, 1453-1461.

22 S. Ramakrishna, A. Le Viet, M. V. Reddy, R. Jose and B. V. R. Chowdari, *J. Phys. Chem. C*, 2010, **114**, 664–671.

23 R. Romero, J. R. Ramos-Barrado, F. Martin and D. Leinen, in *Surface and Interface Analysis*, 2004, **36**, 888–891.

24 M. Aufray, S. Menuel, Y. Fort, J. Eschbach, D. Rouxel and B. Vincent, *J. Nanosci. Nanotechnol.*, 2009, **9**, 4780-4785.

25 R. Yan, G. Khalsa, B. T. Schaefer, A. Jarjour, S. Rouvimov, K. C. Nowack, H. G. Xing and D. Jena, *Appl. Phys. Express*, 2019, **12**, 23008.

26 Z. Li, W. Yang, Y. Losovyj, J. Chen, E. Xu, H. Liu, M. Werbianskyj, H. A. Fertig, X. Ye and S. Zhang, *Nano Res.*, 2018, **11**, 5978–988.

27 E. Asselin, T. M. Ahmed and A. Alfantazi, *Corros. Sci.*, 2007, **49**, 694–710.

28 M. Wahlqvist and A. Shchukarev, *J. Electron Spectros. Relat. Phenomena*, 2007, **156**–**158**, 310–314.

29 Y. Liu, J. Wu, K. P. Hackenberg, J. Zhang, Y. M. Wang, Y. Yang, K. Keyshar, J. Gu, T. Ogitsu, R. Vajtai, J. Lou, P. M. Ajayan, B. C. Wood and B. I. Yakobson, *Nat. Energy*, 2017, **2**, 17127.

30 J. Shi, X. Wang, S. Zhang, L. Xiao, Y. Huan, Y. Gong, Z. Zhang, Y. Li, X. Zhou, M. Hong, Q. Fang, Q. Zhang, X. Liu, L. Gu, Z. Liu and Y. Zhang, *Nat. Commun.*, 2017, **8**, 958.

31 J. Zhang, J. Wu, X. Zou, K. Hackenberg, W. Zhou, W. Chen, J. Yuan, K. Keyshar, G. Gupta, A. Mohite, P. M. Ajayan and J. Lou, *Mater. Today*, 2019, **25**, 28–34.

32 L. Najafi, S. Bellani, R. Oropesa-Nuñez, A. Ansaldo, M. Prato, A. E. Del Rio Castillo and F. Bonaccorso, *Adv. Energy Mater.*, 2018, **8**, 1801764.

33 L. Najafi, S. Bellani, R. Oropesa-Nuñez, M. Prato, B. Martín-García, R. Brescia and F. Bonaccorso, *ACS Nano*, 2019, **13**, 3162–3176.

34 L. Najafi, S. Bellani, R. Oropesa-Nuñez, A. Ansaldo, M. Prato, A. E. Del Rio Castillo and F. Bonaccorso, *Adv. Energy Mater.*, 2018, **8**, 1703212.

35 Z. Zhu, H. Yin, C.-T. He, M. Al-Mamun, P. Liu, L. Jiang, Y. Zhao, Y. Wang, H.-G. Yang, Z. Tang, D. Wang, X.-M. Chen and H. Zhao, *Adv. Mater.*, 2018, **30**, 1801171.